Materials & Design 255 (2025) 114210

Contents lists available at ScienceDirect

Materials & Design

journal homepage: www.elsevier.com/locate/matdes

Additive Manufactured Multi-Material 3D metasurfaces for broadband achromatic electromagnetic focusing

Jiaqi Cai [a,b], Li Deng [a,*], Jiexin Lai [b], Shufang Li [a], Md Ashif Islam Oni [c], Shuvashis Dey [c], Yang Yang [b,**]

[a] School of Information and Communication Engineering,Beijing University of Posts and Telecommunications, Beijing 100876, PR China
[b] School of Electrical and Data Engineering, University of Technology Sydney, NSW 2019, Australia
[c] Department of Electrical and Computer Engineering, North Dakota State University, Fargo, ND 58102, United States

ARTICLE INFO

Keywords:
Metasurfaces
Additive Manufacturing
Broadband Achromatic
Inverse Design
Deep Conditional Generative Adversarial Networks
Electromagnetic Focusing

ABSTRACT

In this paper, a broadband achromatic focusing metasurface design scheme based on the equivalent circuit theory and optimized by a deep learning method is proposed. The designed metasurface element consists of multilayer metal rings and a grounding layer, and the phase modulation effect of achromatic aberration in a wide frequency range is realized by precisely controlling the distance between the layers. The preparation of this complex structure is realized by using additive manufacturing technology, which effectively overcomes the limitations of traditional printed circuit board technology in manufacturing complex structures. To further improve the design efficiency, deep conditional generative adversarial network is introduced in this paper to quickly determine the structural parameters and realize the inverse design, which significantly improves the efficiency and accuracy of the metasurface structure design. The experimental results show that the metasurface possesses good focusing performance in the 17 to 35 GHz band with an effective bandwidth utilization of 69.2 %. The design method proposed in this study combines artificial intelligence and additive manufacturing technology, which provides new design ideas for applications in the fields of communication, optics and wireless energy transmission.

1. Introduction

Metasurfaces are artificial electromagnetic materials that can flexibly control the amplitude, phase, and polarization of electromagnetic waves through a specific periodic arrangement of subwavelength structures [1–3]. Compared with traditional optical components and conventional electromagnetic devices, metasurfaces have become a research direction in the fields of communications and optics in recent years due to their advantages, such as light and thin structure, high design freedom, and strong performance adjustability. In the field of wireless communications, metasurfaces can achieve beamforming and high-efficiency gain of antenna patterns with their wavefront control characteristics, thereby improving the complexity of traditional antenna systems that rely on mechanical or electronic phased arrays [4–7]. Metasurfaces also show advantages in technical directions such as filtering, electromagnetic stealth, and beamforming, providing technical support for the next generation of wireless communication systems [8–11]. In the field of optics, metasurfaces have promoted the development of super-resolution imaging, dynamic holographic technology, and adaptive optical components by controlling the phase of light waves, overcoming many limitations of traditional optical systems in size, integration, and performance [12–14]. At the same time, it also has unique advantages in spectral analysis, polarization modulation, and photonic crystal structure design, and has gradually become an important driving force for innovation in optical technology [15–18].

The practical application of metasurfaces in the fields of communication and optics involves the effective convergence of energy in a specific spatial region, which leads to the concept of electromagnetic focusing. Electromagnetic focusing refers to the use of specific structures to accurately adjust the phase of the incident wavefront so that the electromagnetic energy is accurately concentrated at the target spatial position, thereby improving energy utilization efficiency. This technology is particularly representative in the field of medical imaging and treatment. Methods such as Magnetic Resonance Imaging (MRI) and focused ultrasound therapy are typical applications that use electromagnetic focusing to achieve high-precision imaging and efficient

* Corresponding author: School of Information and Communication Engineering,Beijing University of Posts and Telecommunications, Beijing 100876, PR China.
** Corresponding author: School of Electrical and Data Engineering, University of Technology Sydney, NSW 2019, Australia.
E-mail addresses: dengl@bupt.edu.cn (L. Deng), yang.yang-1@uts.edu.au (Y. Yang).

https://doi.org/10.1016/j.matdes.2025.114210
Received 27 March 2025; Received in revised form 27 May 2025; Accepted 4 June 2025
Available online 9 June 2025

energy transmission [19–22]. In addition, the development of wireless energy transmission in recent years also requires the use of electromagnetic focusing technology to achieve long-distance, low-loss non-contact energy supply. Typical scenarios include wireless charging of electric vehicles, powering of portable devices, and continuous energy supply of IoT devices. This non-contact energy transmission method greatly reduces the dependence on cables and improves the overall flexibility and stability of the energy system [23–26].

In recent years, in response to electromagnetic focusing needs such as imaging and beam shaping, researchers have introduced a variety of broadband achromatic metal lens designs and published rich research results. Mainstream strategies include group delay control, multilayer structure integration, PB phase synthesis, and deep learning-assisted inverse design. Zheng et al. [27] proposed to use the spectral freedom function $C(\omega)$ as an optimization variable to achieve a broadband achromatic metalens with an average transmission efficiency of more than 50 % in the long-wave infrared band. The focal length change is only 4.1 %, which effectively alleviates the focal plane drift problem caused by structural dispersion; Huang et al. [28] used a genetic algorithm based on diffraction theory and combined it with the off-axis optimization target to achieve a single-layer Broadband Achromatic Metalens covering a 40° field of view in the 8–12 μm band, but its average focusing efficiency is still limited by material loss and structure thickness; and Xie et al. [29] proposed a composite metalens structure composed of two types of sub-lenses, concave and convex, based on 3D printing technology. The frequency band covers 50–102 GHz and shows good phase compensation capability, but its structural complexity is high, and processing accuracy and material loss are still one of limiting factors.

Although existing research has achieved relatively controllable dispersion compensation in different frequency bands, how to balance wide bandwidth, high focusing efficiency, manufacturing feasibility and structural simplicity is still a key difficulty in the current metal lens design. In the study of Modified Luneburg Lens [30], the authors achieved sub-diffraction focusing and directional emission capabilities with a FWHM less than 0.4λ by adjusting the radial gradient refractive index, but this structure relies on fine 3D gradient printing and continuous substrate construction, which places high demands on the manufacturing process. Huang et al. [31] used an inverse design algorithm based on particle swarm optimization to achieve focal length offset control within ± 0.5 μm in the near-infrared band, further improving the stability and tolerance of the system imaging.

From the actual design process of metasurfaces, the current traditional methods rely on theoretical derivation, empirical formulas or large-scale parameter scanning. This method has extremely low design efficiency when facing complex multi-dimensional parameter spaces and nonlinear coupling problems, consumes a lot of computing resources and time, and is difficult to obtain a global optimal solution. In recent years, inverse design has been widely proposed. Its characteristic is to first determine the required electromagnetic response target and then reverse solve the geometric structure parameters that meet these requirements. Although this method effectively solves the logical problem from demand to structural design, it still needs to search for the optimal solution in the high-dimensional parameter space. It is usually difficult to balance high precision and high efficiency under limited computing resources, especially when it involves multiple objectives and multiple constraints. To break through the bottleneck of traditional design methods, the emergence of artificial intelligence and deep learning technology has provided a new approach for metasurface inverse design. Machine learning can capture complex and nonlinear implicit associations from massive structural-electromagnetic response data, thereby achieving fast and accurate structural parameter prediction [32–38].

With the development of machine learning, data-driven inverse design has received widespread attention in the field of optoelectronic materials and devices. Compared with traditional empirical scanning or topology optimization methods, machine learning can automatically extract nonlinear mapping relationships from high-dimensional structure-performance data, significantly improve design efficiency and broaden the space of accessible solutions. Zheng et al. used conditional generative adversarial networks to achieve broadband achromatic design of nanocolumn metal lenses in the visible light band, with an average transmission efficiency of more than 50 % [39]; Huang et al. combined the random forest model to propose an incident direction estimation algorithm based on programmable metasurfaces and single detector arrays, achieving high-precision DOA estimation of more than 95 % and an error of less than 0.5° [40]; Lin et al. combined Variational Autoencoders (VAE) with genetic algorithms for complex non-convex optimization of reflective metasurface design, and successfully achieved angle-adjustable scattering enhancement [41]; Xu et al. used Deep Neural Networks (DNNs) to accelerate the inverse design of scattering metasurfaces, significantly shortening the number of simulations [42]. In addition, Zhou et al. introduced a Multilayer Perceptron (MLP) network into the multimode propagation and phase control of the elastic metasurface element, realizing a dual-function design of edge detection and beam deflection [43].

This paper proposes a broadband achromatic electromagnetic focusing metasurface design scheme that combines equivalent circuit theory analysis, additive manufacturing technology and deep conditional generative adversarial network. Specifically, a multi-layered metasurface element is proposed, including two layers of metal rings and a metal substrate. By adjusting the interlayer distance, broadband achromatic phase control is achieved in the 17–35 GHz frequency band. The traditional Printed Circuit Board (PCB) process is limited by the fixed layer spacing design and is difficult to meet the processing requirements of complex three-dimensional structures. The metal-substrate hybrid additive manufacturing technology used in this paper effectively improves the freedom and accuracy of structural manufacturing, breaks through the bottleneck of traditional manufacturing processes, and improves the design accuracy of broadband achromatic phase. To further improve the efficiency and reliability of the inverse design process, we also introduce the Deep Conditional Generative Adversarial Network (DCGAN) algorithm, which can quickly realize the accurate prediction and design optimization of broadband achromatic focusing metasurface structures through a small-scale random sample data set. Both simulation and experimental tests show that the design method proposed in this paper has focusing efficiency in the 17–35 GHz frequency range, and the bandwidth utilization rate reaches 69.2 %. This study combines artificial intelligence with additive manufacturing to provide an efficient design and manufacturing method for metasurface design.

2. Element design theory

As shown in Fig. 1, the metasurface element structure used in this paper consists of two layers of square metal rings and a layer of metal ground plane, which are arranged periodically, with an element period p of 5 mm and a total height h of 2.8 mm. The metal ring width w on the xoy plane is fixed at 0.1 mm, and the metal thickness along the z-axis is fixed at 20 μm. The side lengths of the metal rings are a_1 and a_2, respectively, which can be adjusted in the range of 0.5 mm to 4.9 mm. In the z-axis direction, the distance between the lower metal ring and the ground plane is h_1, the spacing between the upper and lower metal rings is h_2, and the spacing between the upper metal ring and the top of the device is h_3. The sum of the thicknesses of these three dielectric intervals constitutes the total thickness h of the element. By adjusting the values of a_1, a_2, h_1, h_2, and h_3, the reflection phase response of electromagnetic waves at different frequencies can be finely controlled to achieve reflection phase compensation at different frequencies, thereby effectively improving the degree of freedom of achromatic regulation within the bandwidth.

The phase control of the element designed in this paper is achieved

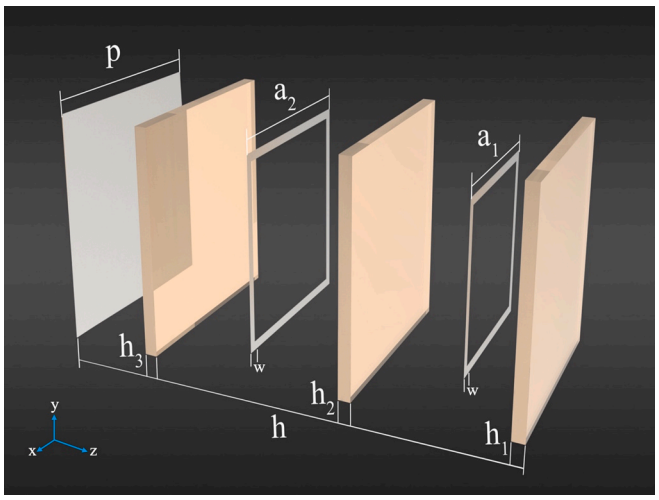

Fig. 1. Achromatic Metasurface Elements using conductive and dielectric multimaterial additive manufacturing.

by adjusting the distance between the metal rings and the side length of the metal rings. The thickness of the metal layer remains consistent during the manufacturing process, thanks to the stability of the additive manufacturing equipment when depositing conductive materials, thus ensuring the consistency and high repeatability of the structural processing process. In this way, not only is the freedom of the element structure in design parameters improved, but also an operational physical basis is provided for subsequent inverse design and rapid printing manufacturing based on machine learning.

In this paper, the metasurface element structures are prepared by additive manufacturing technology, and the substrate material used has a dielectric constant of 2.78 and a loss tangent of 0.018. The preparation process uses Nano Dimension's DragonFly IV additive manufacturing equipment, which, by combining the inkjet printing and photopolymerization processes, can realize the complex electronic components and metasurface structures by combining inkjet printing and photopolymerization processes [44]. The high-precision inkjet print head of this system can precisely deposit liquid materials to form complex 3D structures, and the materials maintain good mechanical stability after curing by ultraviolet (UV) irradiation. DragonFly IV supports the hybrid printing of multiple materials enhances the flexibility of metasurface structure design [45–48].

In the design of broadband achromatic focusing metasurfaces, the key is to accurately control the distance between different layers of metal rings. The PCB usually uses a dielectric board of fixed thickness, which is limited in processing accuracy. When making metasurfaces involving multi-layer structures, it is difficult to meet the high-precision requirements of phase compensation for elements at different positions. Especially under broadband working conditions, a slight deviation may cause the accumulation of phase errors, significantly affecting the overall focusing performance.

In contrast, additive manufacturing technology shows obvious advantages in this scenario. On the one hand, it has higher flexibility in structural design and can flexibly set the distance between metal layers according to the needs of different elements; on the other hand, its manufacturing accuracy is significantly better than that of traditional PCBs, and the material stacking thickness can be stably controlled within the micron level, thereby ensuring the uniformity and repeatability of focusing performance. Specifically in this work, by adjusting the dielectric thickness between metal rings layer by layer, corresponding phase compensation is applied to elements in different areas of the array, achieving a relatively stable focusing response within the frequency band. As shown in Fig. 2, a three-dimensional cross-section diagram of the designed metasurface is shown. Metal rings are

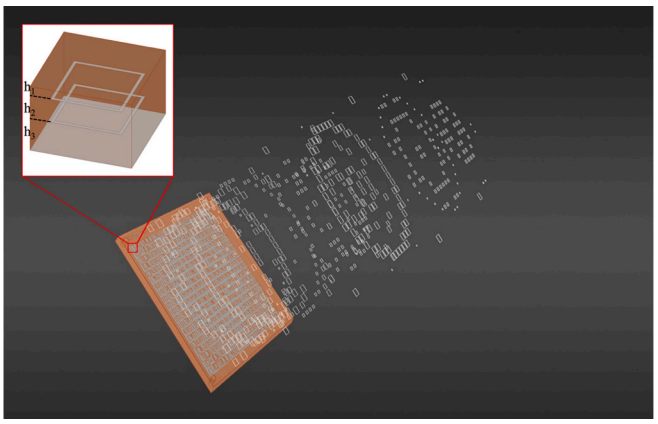

Fig. 2. Schematic distribution of three-dimensional structures on a broadband achromatic metasurface designed by a deep conditional generative adversarial network algorithm.

embedded at different heights in the substrate, and their position differences are used to finely adjust the reflection phase. This multi-layer embedded structure breaks the limitations of traditional planar processing, not only ensuring the compactness of the device, but also leaving ample parameter adjustment space for subsequent reverse optimization.

However, the structural complexity brought about by additive manufacturing also leads to an increase in the number of metal layers in the metasurface element, raising the need for computation in the design process. Although the traditional parameter scanning method can be used to optimize the structural design, the increase in parameters such as the metal ring edge length and the metal ring layer spacing of the metasurface element leads to the excessive computational burden of the traditional design method, and the optimization process is time-consuming, consumes many computational resources, and is less efficient. To improve this problem, this paper introduces the deep learning technology to quickly obtain the structural parameters that satisfy the target electromagnetic performance requirements through the deep learning model, which significantly improves the design efficiency and solves the problems existing in the traditional methods.

As shown in Fig. 3, according to the Transmission Line Theory (TLM), the equivalent impedance Z_{MS} of the metasurface element is determined by the metallic ring structure and the thickness of the dielectric layer, while the characteristic impedance Z_h of the dielectric depends on the chosen dielectric material. The metal grounding layer is theoretically considered as an ideal short circuit, and therefore its equivalent impedance Z_g is 0 [49].

The transmission characteristics of the metasurface element can be represented by the *ABCD* matrix as follows:

$$\begin{pmatrix} A & B \\ C & D \end{pmatrix} = \begin{pmatrix} \cosh\gamma h & Z_h \sinh\gamma h \\ \frac{1}{Z_h}\sinh\gamma h & \cosh\gamma h \end{pmatrix} \tag{1}$$

where h is the thickness of the dielectric, γ is the propagation constant, and Z_h is the characteristic impedance of the dielectric.

The reflectivity Γ of the element can be calculated by the following equation (2):

$$\Gamma = \frac{Z_{MS} - Z_0}{Z_{MS} + Z_0} \tag{2}$$

where Z_0 is the characteristic impedance of air. Since the metal grounding layer is regarded as a lossless ideal short circuit, its impedance Z_g is 0. By adjusting the parameters of the metasurface element (h_1, h_2, h_3), the value of Z_{MS} can be varied to realize the control of the reflection phase.

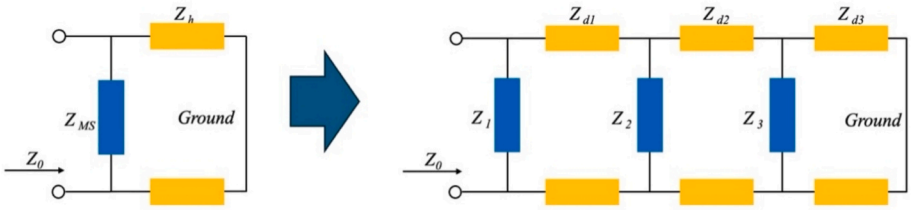

Fig. 3. Equivalent circuit theory for impedance calculation of metasurface elements.

In the multilayer structure design, the equivalent circuit model of the metasurface element contains multiple dielectric layers (Z_{d1}, Z_{d2}, Z_{d3}) and the characteristic impedance of the multilayer metasurface structure (Z_1, Z_2, Z_3). By finely adjusting the heights between the metal rings (h_1, h_2, h_3), the characteristic impedance of each layer can be varied to achieve more precise control of reflection phase and achromatic phase.

The equivalent impedance Z_{eq} of the multilayer structure can be expressed as:

$$Z_{eq} = Z_1 \| Z_2 \| Z_3 \tag{3}$$

where the equivalent impedance Z_{eq} is the result of the parallel connection of the impedances of each layer. The importance of the multilayer design is that it can provide richer phase regulation capability and more effectively realize the fine regulation of phase response and dispersion.

As shown in Fig. 4, six different parameter combinations of metasurface elements (a_1, a_2, h_1, h_2) were selected, and the reflection phase curves of each metasurface element were simulated using ANSYS HFSS simulation software. The simulation results show that the characteristic impedance of the metasurface can be effectively changed by adjusting these geometrical parameters, thus realizing a rich control of the phase response and dispersion characteristics over a wide frequency range from 17 GHz to 35 GHz. The importance of multilayer design in the design of broadband metasurfaces is further verified, and the feasibility of utilizing additive manufacturing to realize this structure is also demonstrated.

3. Array design theory

In the design of wideband achromatic reflectarray antennas, it is necessary to solve the dispersion problem encountered by conventional reflectarray antennas under wideband operating conditions [50]. The traditional reflectarray antenna will cause the propagation direction of the reflected wave in space to change with frequency due to the inconsistency of the reflection paths of electromagnetic waves of different frequencies, which will cause the focal point positions of electromagnetic waves of different frequencies to be unable to coincide, directly reducing the focusing effect of the antenna in the broadband. This dispersion phenomenon is especially obvious when the operating band is wide.

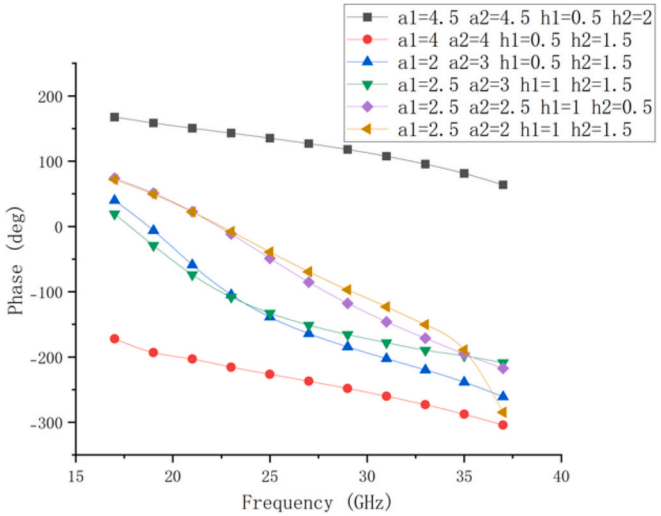

Fig. 4. Phase curves of achromatic metasurface elements.

The traditional reflectarray antenna has the best gain and focusing performance at the center frequency f_C, but when the operating frequency deviates from the center frequency, such as the lower frequency f_L or higher frequency f_H shown in Fig. 5(a), the phase distribution of the reflected wave changes, resulting in a decrease in focusing performance. This is since the phase center of a conventional reflectarray antenna is shifted with frequency changes, creating a dispersion effect. The dispersion phenomenon not only limits the bandwidth of the antenna, but also significantly reduces the high gain performance in a wide frequency band.

Taking the traditional horn antenna feed as an example, due to the fixed position of the phase center of the horn antenna, it is difficult to adjust the traditional reflectarray antenna for phase changes at different frequencies. This makes the reflectarray antenna can only achieve the ideal focusing effect at a single pre-designed frequency f_C, while the focusing ability is significantly reduced at other frequencies. Therefore, effectively solving the dispersion problem and realizing high-performance focusing under wideband operation have become important challenges in designing wideband achromatic reflectarray antennas [51,52].

Different from the traditional reflectarray antenna, the achromatic reflectarray antenna adopts a phase modulation scheme with low dispersion, which effectively reduces the phase difference between electromagnetic waves of different frequencies. As shown in Fig. 5(b), the design enables electromagnetic waves of different frequencies to be focused to the same spatial location, resulting in a stable high-gain performance over a wide frequency range.

The achromatic reflection array replaces the conventional dispersion-type reflection surface by introducing a frequency-independent phase compensation structure. By optimizing the parameters of the metasurface element, the phase response of the element is realized to be highly consistent throughout the entire operating frequency band, effectively eliminating the dispersion problem brought about by frequency changes.

In the design of this paper, the horn antenna as the electromagnetic wave feeder is placed at a position about 100 mm away from the metasurface array. The electromagnetic wave emitted by the horn antenna is a spherical wave, and the metasurface array firstly needs to compensate the phase of the spherical wave to convert it into a plane wave, and then further carry out the phase control to precisely focus the plane wave to the focal point position of 300 mm.

The phase distribution of a spherical wave transmitted by a horn antenna can be expressed as:

$$\Phi_{spherical}(r,f) = \frac{2\pi}{\lambda(f)}\left(\sqrt{r^2+d^2} - d\right) \tag{4}$$

where $\Phi_{spherical}(r,f)$ is the phase distribution at frequency f, r is the radial

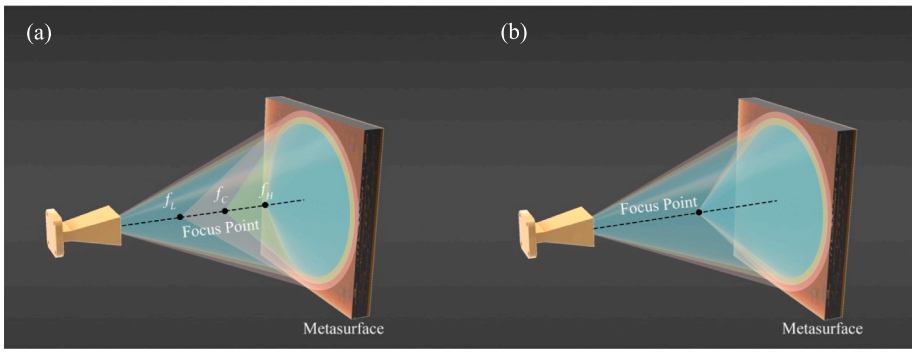

Fig. 5. Comparison of focusing effect between broadband achromatic antenna and conventional reflector array antenna.

distance from the metasurface element to the focal point, d is the distance from the horn antenna to the metasurface, and the wavelength $\lambda(f) = \frac{c}{f}$, with c being the speed of light.

To realize the transformation from spherical to plane waves, the metasurface needs to impose the corresponding phase compensation:

$$\Phi_{compensation}(r,f) = -\frac{2\pi}{\lambda(f)}\left(\sqrt{r^2+d^2} - d\right) \tag{5}$$

After this compensation, the spherical wave can be transformed into a plane wave after passing through the metasurface.

To realize the focusing effect, the metasurface also needs to further adjust the phase of the plane wave, so that it is focused on the focal point of 300 mm from the array. According to the lens focusing principle, the phase distribution of the metasurface needs to satisfy:

$$\Phi_{focusing}(r,f) = \frac{2\pi}{\lambda(f)}\left(\sqrt{r^2+F^2} - F\right) \tag{6}$$

where F is the focal length and r is still the radial distance from the element to the focal point.

In the actual design, the spherical wave phase compensation and focusing phase modulation are integrated on the same metasurface array, and each metasurface element must satisfy the above two demands at the same time, so the overall phase modulation of the metasurface element can be expressed as:

$$\Phi_{total}(r,f) = \Phi_{compensation}(r,f) + \Phi_{focusing}(r,f) \tag{7}$$

which simplifies to:

$$\Phi_{total}(r,f) = \frac{2\pi}{\lambda(f)}\left(\sqrt{r^2+F^2} - F - \sqrt{r^2+d^2} + d\right) \tag{8}$$

Eq. (8) for the metasurface element simultaneously realizes the phase compensation of spherical wave and the phase modulation of plane wave focusing.

To realize the broadband focusing effect, the metasurface needs to maintain a stable phase response throughout the operating frequency band. In this study, the phase response of the metasurface is optimized at the center frequency f_C to ensure that the phase response at this frequency is ideal. At higher frequency f_H and lower frequency f_L, the phase response of the element is affected by the wavelength change, but by adjusting the structural parameters of the metasurface element, the phase response can be controlled at the corresponding phase in a wide frequency range, thus realizing the achromatic focusing performance on a wide band.

To verify the design theory of the wideband achromatic reflectarray proposed in this paper, an achromatic reflectarray antenna with a diameter of 80 mm is designed, the feed is a horn antenna, the feed is 100 mm away from the metasurface reflectarray, and the target focus is located at a position of 300 mm from the metasurface reflectarray. Fig. 6 shows the required phase distribution of each metasurface element in the 20 × 20 array, where the blue curve indicates the focusing phase requirement at the frequency of 17 GHz, the red curve indicates the phase requirement at the frequency of 35 GHz, and the yellow shaded area demonstrates the distribution of the required phases of the metasurface elements in the range of the frequency band from 17 to 35 GHz.

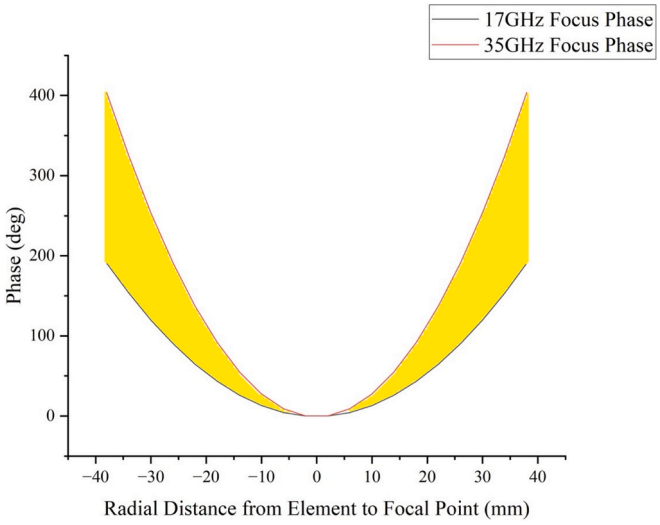

Fig. 6. Phase distribution requirements for each metasurface element of a 20 × 20 array.

4. Generative adversarial networks

In the design of broadband achromatic reflector array antennas, it is critical to establish a comprehensive library of metasurface elements with diverse parameters. However, the relationship between the structural parameters of the metasurface and its electromagnetic response is very complex and highly nonlinear. Traditional methods generally optimize the structural parameters step-by-step through many simulations and experiments to match the target electromagnetic performance. Although this method is effective, it is inefficient, time-consuming and consumes many computational resources, which makes it difficult to meet the current demand for rapid design of metasurfaces.

To address this problem, this paper proposes an inverse design method based on DCGAN, which generates the corresponding structural parameters directly from the given target electromagnetic response. The DCGAN model consists of a Generator and a Discriminator. The Generator is responsible for learning the mapping relationship from the electromagnetic response to the structural parameters, while the Discriminator continuously optimizes the quality of the Generator's output by distinguishing the generated data from the real data [53]. In this paper, we train the DCGAN model with simulation data and verify

its effectiveness in inverse design of metasurface elements. Compared with traditional methods, deep learning-based inverse design not only improves the design efficiency but also enhances the design accuracy.

The DCGAN network structure designed in this paper is shown in Fig. 7 for the inverse design of metasurface elements. Unlike traditional GAN models, both the generator and discriminator in this study incorporate additional conditional information y, so that the network output depends not only on the random noise z, but also on the input broadband achromatic phase conditions φ_1, φ_2, φ_3, φ_4, φ_5, φ_6, φ_7. These phase conditions correspond to seven representative frequency points in the frequency band at 17 GHz, 20 GHz, 23 GHz, 26 GHz, 29 GHz, 32 GHz, and 35 GHz, which are used to generate the corresponding metasurface structure parameters [a_1, a_2, h_1, h_2]. In the network structure, the generator and the discriminator are based on the MLP model of the fully connected network.

The inputs to the generator include random noise z and conditional phase $y = [\varphi_1, \varphi_2, \varphi_3, \varphi_4, \varphi_5, \varphi_6, \varphi_7]$. The random noise z obeys a uniform distribution $U(-1,1)$ with a dimension of 100×1; the conditional phase is the broadband achromatic aberration phase obtained by simulating the metasurface element, with a dimension of 7×1. Therefore, the generator has a total dimension of 107×1 for the inputs and 4×1 for the outputs, which corresponds to the structural parameters [a_1, a_2, h_1, h_2].

To better capture the nonlinear relationship between the achromatic phase and the structural parameters, the generator adopts a network structure containing an input layer, two hidden layers and an output layer, as shown in Table 1.

The goal of the generator is to learn the characteristics of the joint distribution of random noise z and conditional phase y, and generate structural parameters [a_1, a_2, h_1, h_2] that satisfy the target conditions.

The input to the discriminator then consists of the generated structural parameters or the true structural parameters, and the corresponding phase conditions, combined into an 11×1 dimensional vector. The discriminator consists of one input layer, four hidden layers and one output layer, and its output is a scalar representing the probability that the input structural parameters are real data. The specific structure of the discriminator is shown in Table 2.

The discriminator discriminates between true and generated structural parameters as accurately as possible, thus improving the accuracy of the discrimination. The training objective is to maximize the probability that the real parameters are discriminated as true and minimize the probability that the generated parameters are discriminated as true.

The hidden layers of both the generator and the discriminator use a nonlinear Rectified Linear Element (ReLU) activation function with the expression:

$$f(x) = max(0, x) \tag{9}$$

The ReLU activation function can effectively alleviate the gradient vanishing problem and speed up the network training. Meanwhile, the generator output layer uses Tanh activation function:

Table 1
Generator Network Structure.

Layer	Number of Neurons	Activation Function
Input Layer	107	None
Hidden Layer 1	256	ReLU
Hidden Layer 2	128	ReLU
Output Layer	4	Tanh

Table 2
Discriminator Network Structure.

Layer	Number of Neurons	Activation Function
Input Layer	11	None
Hidden Layer 1	128	ReLU
Hidden Layer 2	64	ReLU
Hidden Layer 3	32	ReLU
Hidden Layer 4	16	ReLU
Output Layer	1	Sigmoid

$$f(x) = \frac{e^x - e^{-x}}{e^x + e^{-x}} \tag{10}$$

The Tanh function restricts the generator output range to between [-1,1], corresponding to the range after normalization of the structural parameters.

The DCGAN model training is done using an adversarial game, defining the loss function as:

$$L = \min_G \max_D \left(\mathbb{E}_{(x,y)\sim p_{data}} [\log D(x|y)] + \mathbb{E}_{z\sim p_z(z)} [\log(1 - D(G(z|y)|y))] \right) \tag{11}$$

where $logD(a_1, a_2, h_1, h_2|y)$ represents the discriminator's loss for real structural parameters, and $log(1 - D(G(z|y)|y))$ represents the discriminator's loss for generated structural parameters. Alternate training by minimizing the generator loss and maximizing the discriminator loss makes the generator gradually generate more realistic structural parameters.

To evaluate the performance of the DCGAN model, the training set contains 10,000 sets of samples, which are divided into training sets and test sets in a ratio of 9:1. The training set is used for model training, and the test set is used to evaluate its inversion design capabilities. The prediction accuracy of the generator was quantified by calculating the Expected Root Mean Square Error (ERMSE) and Expected Maximum Error (EMAXE) between the generated and real structural parameters.

The ERMSE is defined as:

$$E_{RMSE} = \sqrt{\frac{1}{m}\sum_{i=1}^{m} (\hat{y}_i - y_i)^2} \tag{12}$$

The EMAXE is defined as:

$$E_{MAXE} = max|\hat{y}_i - y_i| \tag{13}$$

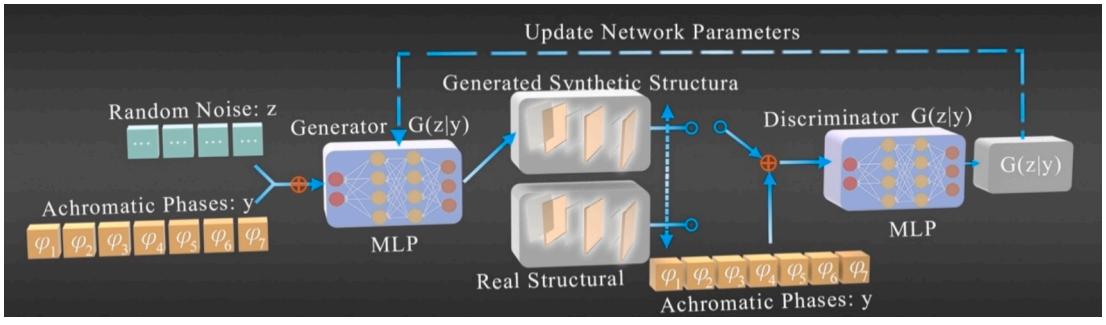

Fig. 7. Schematic of the DCGAN network-based model for inverse design of metasurface.

where $\hat{a}_i$ is the i^{th} point of the generated structural parameters, and a_i is the i^{th} point of the real structural parameters. These evaluation metrics effectively assess the inverse design capability of the DCGAN model.

The DCGAN model uses a generator and discriminator, both with a learning rate of 0.001. Additionally, the regularization coefficient for the weights of each fully connected layer is set to 0.001, with training running for 10×10^4 epochs. As shown in Fig. 8(a), during the training process, the loss function values of the generator and the discriminator gradually converge, indicating that the adversarial game between them gradually reaches equilibrium. Initially, the generator outputs structural parameters of low quality, which are easily recognized by the discriminator, and thus the loss is high. As the training advances, the quality of the generator output gradually improves, and it is gradually difficult for the discriminator to distinguish between real and generated data, so that the loss of the generator is gradually reduced and stabilized. At this point, the discriminator accuracy is close to random guessing (about 50 %), proving that the generator has successfully captured the complex mapping relationship between the structural parameters and the electromagnetic response, meeting the design goal.

To verify the effectiveness of the proposed DCGAN-based inverse design method for metasurface elements, the noise dimension was fixed at 100×1 during testing. Then, 100 sets of achromatic phases [φ_1, φ_2, φ_3, φ_4, φ_5, φ_6, φ_7] from the test set were input into the trained generator, which predicted the corresponding structural parameters [a_1, a_2, h_1, h_2]. To quantitatively evaluate the prediction error in the inverse design of metasurface elements, the ERMSE and EMAXE were calculated to measure the gap between the generator's output structural parameters and the real simulation data. According to equations (12) and (13), the predicted root mean square error for the metasurface element is 0.12 %, and the maximum error is 0.38 %, achieving a prediction accuracy of 99.88 %.

As shown in Fig. 8(b), it is a prediction error histogram of DCGAN-based inverse design. Despite the high overall accuracy, there are still relatively large errors in individual points, mainly for two reasons. First, although the training samples cover the main structural response distribution, there are still a small number of sparse areas in phase space, especially at the locations where the phase changes drastically at the edge of the bandwidth. When the test points happen to fall into these areas, the generator can only rely on adjacent points for interpolation estimation, resulting in a slight increase in local errors. Second, there are certain high-order coupling relationships between structural parameters, this nonlinear interaction is difficult to fully capture with a neural network under limited training samples. The current model mainly learns significant first-order trends, while some coupling terms have not been fully expressed. Therefore, when multiple parameters change significantly at the same time, the prediction deviation is relatively higher. The above analysis explains the causes of individual outliers in Fig. 8(b) and further reveals potential optimization directions for improving the accuracy of inverse design.

The computational efficiency advantage of the DCGAN model over the traditional parameter scanning method is significant, with the computation time for each inverse design taking only 19 ms. Traditional methods usually take hours or even longer for the complete simulation and optimization process, so the DCGAN inverse design method proposed in this paper improves the design efficiency.

5. Experimental testing and discussion

As shown in Fig. 9, the experimental sample is a 20×20 metasurface element array, which was prepared using the DragonFly IV additive manufacturing system from Nano Dimension. This advanced manufacturing technology is capable of processing complex structures with high precision, ensuring the consistency and stability of the metasurface array in terms of design size and processed structure.

To verify the actual performance of the designed broadband achromatic focused metasurface arrays, we carried out experimental tests in the 17–35 GHz band range. As shown in Fig. 10, the experimental setup used a cross-programmable test system equipped with two ERAVANT WR-42 SAR-1532–42-S2 horn antennas for electromagnetic wave transmission and reception. The metasurface array was placed about 100 mm in front of the transmitting antennas to receive the incident wave at an inclination angle of 15°, and the reflected wave left the metasurface array at a direction of −15° and achieved focusing on a position 300 mm away from the array. During the experimental test, the receiving antenna is placed at the focal position 300 mm from the array, and scanning measurements are performed in the near-field region to obtain the electric field strength of the reflected electromagnetic waves at different frequencies, to analyze the focusing performance of the metasurface array in a wide frequency band.

As shown in Fig. 11, the full-wave simulation of the designed achromatic metasurface array was carried out by using the high-frequency electromagnetic simulation software of ANSYS HFSS, and the simulation band covered 17–35 GHz. at seven representative frequency points, namely 17 GHz, 20 GHz, 23 GHz, 26 GHz, 29 GHz, 32 GHz and 35 GHz, the simulation results showed that the electromagnetic waves were all focused on a wide band. The simulation results show that the electromagnetic waves are effectively focused on the same spatial position, indicating that the designed metasurface array can realize relatively stable focusing performance on a wide frequency range. However, as the frequency approaches 35 GHz, the dispersion effect at both ends begins to appear, and although the focusing performance decreases, it can still form an obvious electromagnetic focusing point.

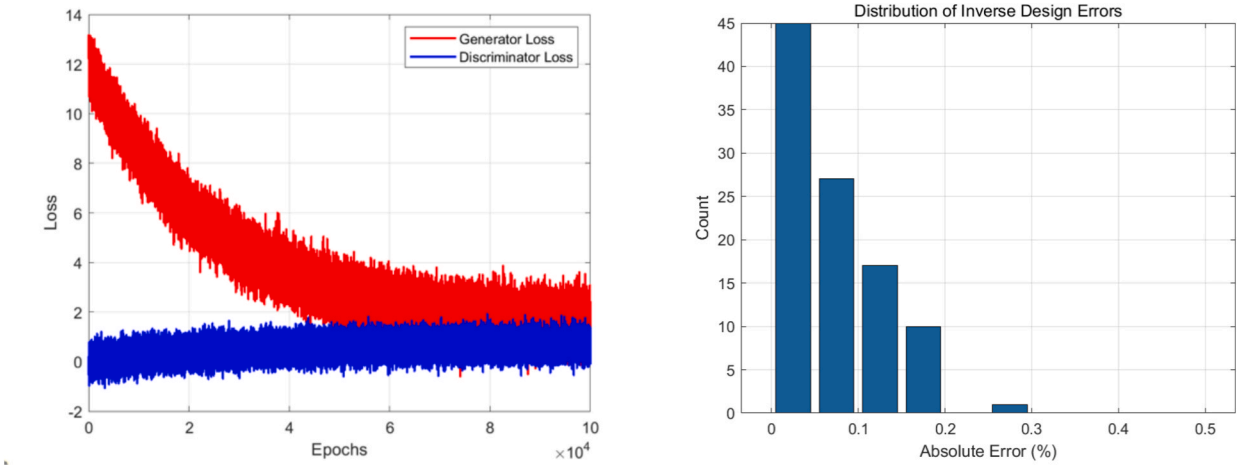

Fig. 8. (a)Loss function curves of DCGAN generator and discriminator. (b) Prediction error histogram of DCGAN-Based Inverse Design.

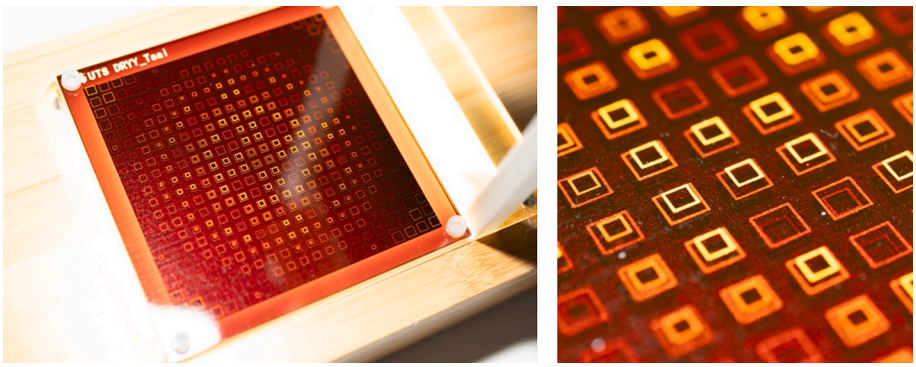

Fig. 9. Wideband achromatic metasurface arrays prepared by additive manufacturing (the metal rings of each metasurface element have different heights within the substrate).

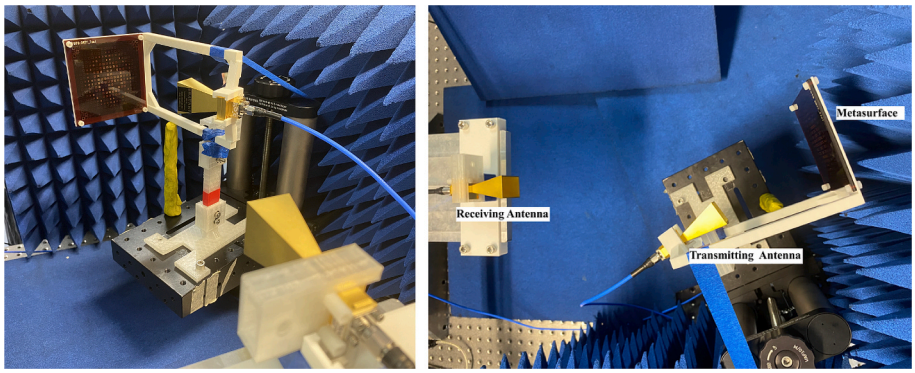

Fig. 10. Experimental setup diagram for near-field planar scanning measurement (cross-programmable test system).

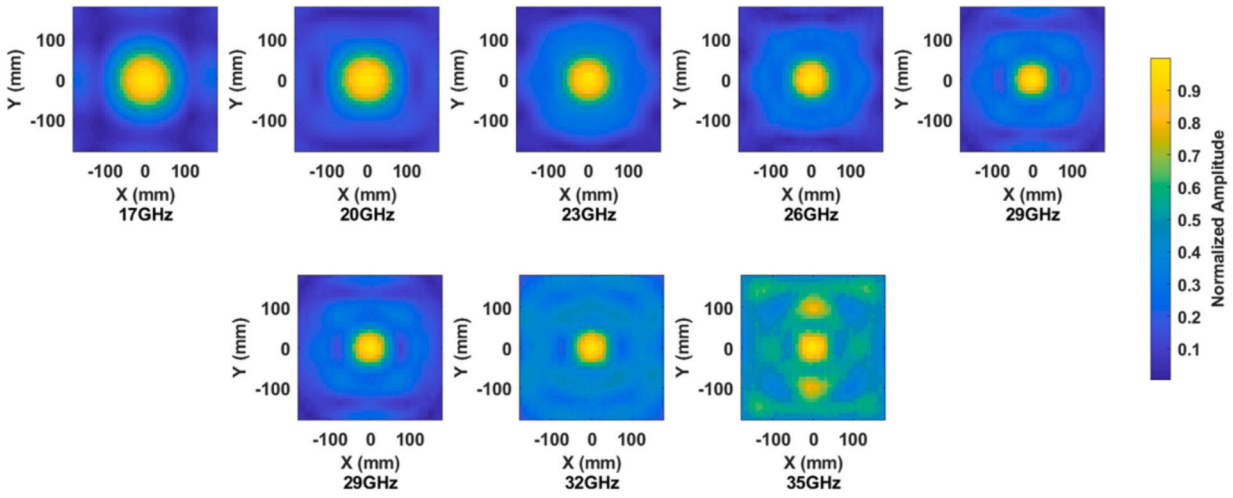

Fig. 11. Simulated amplitude distribution of the electric field focused by the metasurface array.

As shown in Fig. 12, the scanning results of the experimentally measured near-field electromagnetic wave field strength in the frequency range of 17–35 GHz are shown. To facilitate the comparative analysis of the focusing performance at different frequencies, we have normalized the scanning results. The experimental results show that the designed metasurface array can effectively focus the reflected wave at the preset 300 mm focal point over a wide frequency range from 17 GHz to 35 GHz, and the experimental measurements are in good agreement with the simulation results. Especially near the center frequency of 26 GHz, the metasurface array has the best focusing effect, and the reflected wave energy is highly concentrated, showing obvious focusing characteristics. At the edge of the frequency range, 17 GHz and 35 GHz, although the focusing performance is slightly reduced, the energy concentration remains high, which indicates that the designed metasurface array has good performance and stable focusing ability over the whole wide frequency band.

During the additive manufacturing process of the sample, the DragonFly IV process will bring micron-level dimensional tolerances, and slight deviations in the element geometry will disturb the phase compensation and affect the final focus. Taking 35 GHz as an example, the slight offset of the local size causes the measured focus position to differ from the simulation value; however, the phase between adjacent

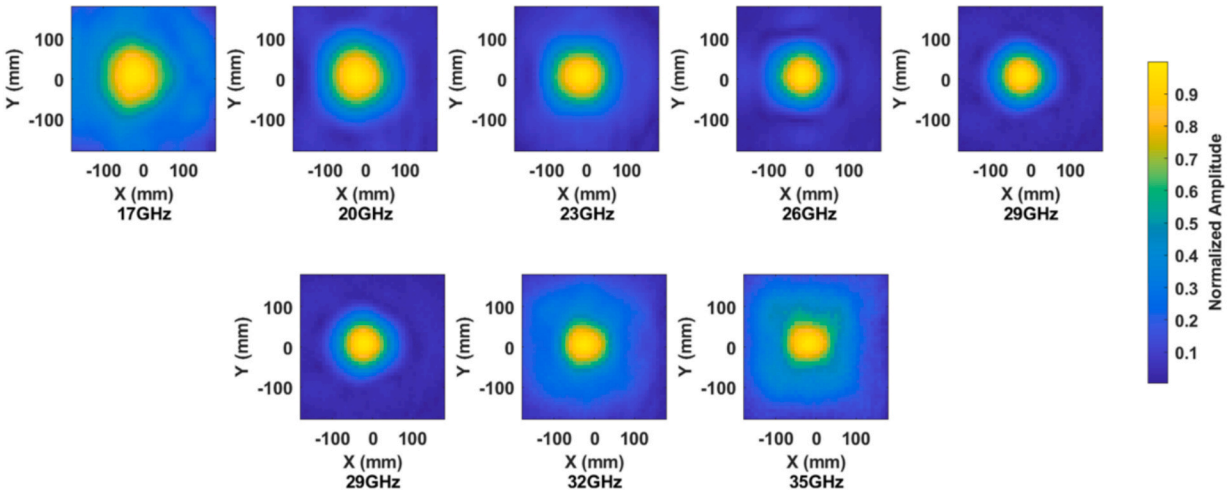

Fig. 12. Measured amplitude distribution of the electric field focused by the metasurface array.

elements has a certain complementary effect in the physical structure, so the measured focus spot is not obviously distorted. Secondly, the original simulation assumes that the substrate dielectric constant is independent of frequency, while the actual material has a slight dispersion in the high-frequency band, which will change the reflection phase and correct the focusing intensity, making the measured results closer to the simulation. Finally, the probe positioning accuracy of the near-field scanning system is about ± 0.5 mm, and the averaging effect of spatial sampling will make the measured field distribution slightly smooth and raise the peak amplitude to a certain extent, thereby masking the slight attenuation predicted in the simulation. The above three points can explain the difference between simulation and experiment near 35 GHz.

To quantify the focusing stability of the metasurface in the entire frequency band, we define the Effective Bandwidth Utilization η, which is expressed as follows [54]:

$$\eta = \frac{f_H - f_L}{f_C} \times 100\% \tag{14}$$

where f_H and f_L are the upper and lower limits of the frequency band for maintaining good focusing performance, and f_C is the center frequency with the best focusing performance. In this work, the three values are: $f_H = 35$ GHz, $f_L = 17$ GHz, $f_C = 26$ GHz we can calculate $\eta = \frac{35-17}{26} \times 100\% = 69.2\%$. The metasurface designed in this paper can maintain stable focusing ability on the frequency band of 17–35 GHz and has excellent broadband achromatic control effect.

To further quantitatively evaluate the focusing ability of the metasurface designed in this paper in the entire 17–35 GHz operating frequency band, based on the measured near-field amplitude distribution shown in Fig. 12, this paper introduces typical performance indicators: focusing radius R_f, focusing efficiency ζ and equivalent Numerical Aperture (NA) to quantitatively analyze the focusing ability.

The focusing radius R_f is used to characterize the spatial compactness of the focusing point. It is defined as: the equivalent radius formed by the point with the maximum amplitude at the focus as the center and the position where the amplitude decays to $1/\sqrt{2}$ (i.e. − 3 dB) as the boundary. In the measured data at 26 GHz, the normalized maximum field strength is about 0.998, the − 3 dB threshold is about 0.707, and the corresponding equivalent focusing radius is $R_f \approx 9.5$ mm. This value is only about 0.83 times the central wavelength $\lambda \approx 11.5$ mm, and the corresponding 3 dB focusing spot diameter is 0.064λ, indicating that the designed array has sub-wavelength focusing capability.

To quantitatively evaluate the energy focusing capability at different frequencies, this paper introduces the focusing efficiency ζ, which is defined as the ratio of the energy in the focal area to the total energy on the entire observation surface [55]. According to Poynting's theorem, the focusing efficiency can be expressed as:

$$\zeta = \frac{P_{Foci}}{P_S} = \frac{Re \oint_{S_{Foci}} (E \times H^*) \bullet dS}{Re \oint_{S} (E \times H^*) \bullet dS} \tag{15}$$

where P_{Foci} is the energy in the circular area S_{Foci} with radius R_f and the focus as the center, and P_s is the total energy on the entire observation surface S.

In the actual calculation, the experiment uses the amplitude data of 40 × 40 grids for calculation, where the observation surface size is 176 mm × 176 mm, and the single point spacing is 4.4 mm. To simplify the calculation, $|E|^2$ is used to approximate the power density, that is:

$$\zeta \approx \frac{\sum_{|E| \geq E_{th}} |E|^2}{\sum_{all} |E|^2} \tag{16}$$

$$E_{th} = \frac{E_{max}}{\sqrt{2}} \tag{17}$$

According to the above formula, the focusing efficiency at each frequency point is shown in Table3.

As shown in Fig. 13, the focusing efficiency of the broadband achromatic metasurface designed in this paper shows good in-band stability at different frequencies. In the main operating frequency band of 20–30 GHz, the focusing efficiency ζ is always maintained between about 48 %–52 %, which fully verifies the broadband achromatic characteristics of its design. After the frequency exceeds 32 GHz, the focusing efficiency decreases to a certain extent due to the enhanced dispersion effect of the array element, which is in line with the expected frequency response trend.

Based on geometric optics approximation, this paper introduces NA as an evaluation indicator to measure the energy focusing ability. It is defined as:

$$NA = \sin\theta_{max} \tag{18}$$

Table 3
Focusing Efficiency ζ (%) Measured at Representative Frequencies from 17 GHz to 35 GHz.

Frequency (GHz)	17	20	23	26	29	32	35
ζ (%)	38.05	52.20	48.11	51.83	52.57	37.19	21.85

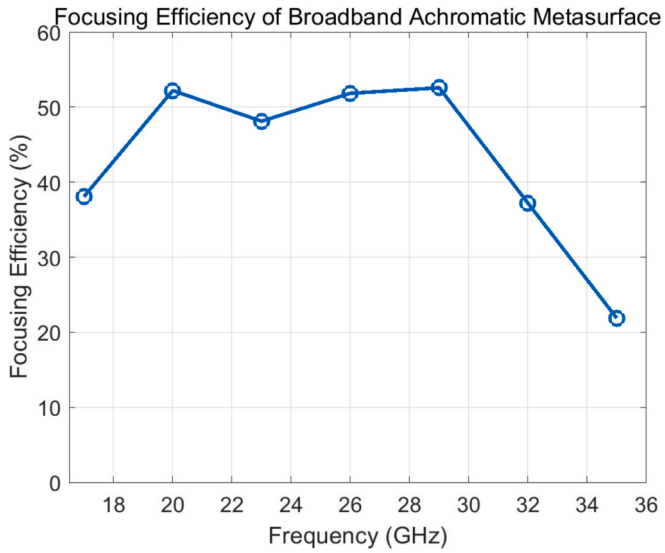

Fig. 13. Frequency-Dependent Focusing Efficiency of Broadband Achromatic Metasurface.

$$\theta_{max} = \tan^{-1}\left(\frac{D/2}{F}\right) \tag{19}$$

where array aperture $D = 80$ mm, focal length $F = 300$ mm, substitute and calculate: $\theta_{max} \approx \tan^{-1}(0.1333) \approx 7.6^{\circ}$, $NA \approx \sin(7.6^{\circ}) \approx 0.132$.

Despite the compact size and relatively long focal length of the proposed structure, efficient energy concentration can be achieved. This design lays a practical foundation for beam focusing and steering in broadband applications.

6. Conclusion

In this paper, we propose a wideband achromatic metasurface element design method based on equivalent circuit theory and successfully realize efficient electromagnetic focusing on a wide frequency range by deep learning-driven inverse design. First, we design a metasurface element with a multilayer structure and realize wideband achromatic focusing on the frequency band from 17 GHz to 35 GHz by reasonably adjusting the geometrical parameters and material properties of the element. The designed element can effectively compensate for the phase response at different frequencies to ensure the consistency of the phase characteristics over a wide frequency range. The experimental results show that the metasurface exhibits the best focusing performance at the center frequency of 26 GHz and maintains a high energy concentration throughout the entire operating band, with its effective bandwidth utilization reaching 69.2 %.

Secondly, this paper introduces a DCGAN for the inverse design of metasurface elements. Compared with the traditional parameter scanning design method, DCGAN dramatically improves the efficiency and accuracy of metasurface design by learning the complex nonlinear mapping between electromagnetic response and structural parameters. In both simulation and experiment, the DCGAN model can generate structural parameters that satisfy the target electromagnetic response in a short time, with an average prediction accuracy of 99.88 %. In addition, the high degree of consistency between experimental measurement data and simulation results further validates the effectiveness of the proposed method.

In this paper, a wideband achromatic metasurface design method that integrates multilayer structure design, deep learning inverse design and additive manufacturing technology is proposed. The method provides a new approach for the fast inverse design of wideband achromatic metasurface, effectively improves the efficiency and accuracy of the metasurface structure design and shows good application prospects in the fields of wireless communication, radar detection and medical imaging.

CRediT authorship contribution statement

Jiaqi Cai: Writing – original draft, Validation, Methodology, Investigation, Formal analysis, Data curation, Conceptualization. **Li Deng:** Writing – review & editing, Supervision, Resources, Data curation, Conceptualization. **Jiexin Lai:** Validation, Methodology, Data curation. **Shufang Li:** Supervision, Funding acquisition. **Md Ashif Islam Oni:** Validation, Investigation. **Shuvashis Dey:** Investigation. **Yang Yang:** Writing – review & editing, Supervision, Project administration, Methodology, Investigation, Funding acquisition, Formal analysis, Conceptualization.

Declaration of competing interest

The authors declare that they have no known competing financial interests or personal relationships that could have appeared to influence the work reported in this paper.

Acknowledgements

This research was funded by the Beijing Natural Science Foundation (Grant Nos. L223030 and L233002), the Australian Research Council Linkage Projects (LP210300004 and LP230200030), the National Science Foundation (Grant No. 2320798), and the China Scholarship Council (Grant No. 202206470026).

Data availability

Data will be made available on request.

References

[1] J. Hu, S. Bandyopadhyay, Y. Liu, L. Shao, A review on Metasurface: from principle to Smart Metadevices, Front. Phys. 8 (Jan. 2021), https://doi.org/10.3389/fphy.2020.586087.
[2] C. Wang, H.-X. Xu, Y. Wang, G. Hu, H. Luo, K. Wang, Reconfigurable transmissive metasurface synergizing dynamic and geometric phase for versatile polarization and wavefront manipulations, Mater. Des. 225 (Jan. 2023) 111445, https://doi.org/10.1016/j.matdes.2022.111445.
[3] F. Faraz, et al., Multi-fold geometric phase metasurface with versatile operations for transmission and reflection, Mater. Des. 243 (Jun. 2024) 113090, https://doi.org/10.1016/j.matdes.2024.113090.
[4] L. Xu, D.Y. Wang, X.G. Zhang, L. Bai, W.X. Jiang, T.J. Cui, Cloud-connected networked Metasurfaces for online electromagnetic manipulations, ACS Photonics 10 (5) (Apr. 2023) 1558–1565, https://doi.org/10.1021/acsphotonics.3c00180.
[5] Z. Xu, et al., Controllable amplified photonic topological insulators for new-architecture Wireless systems, ACS Photonics (Sep. 2024), https://doi.org/10.1021/acsphotonics.4c01147.
[6] J. Wang, et al., Metantenna: when Metasurface meets antenna again, IEEE Trans. Antennas Propag. 68 (3) (Mar. 2020) 1332–1347, https://doi.org/10.1109/tap.2020.2969246.
[7] G.-B. Wu, et al., A universal metasurface antenna to manipulate all fundamental characteristics of electromagnetic waves, Nat. Commun. 14 (1) (Aug. 2023) 5155, https://doi.org/10.1038/s41467-023-40717-9.
[8] M. Li, J. Cai, L. Deng, X. Li, F. Iacopi, Y. Yang, Additively manufactured conductive and dielectric 3D metasurfaces for independent manipulation of broadband orbital angular momentum, Mater. Des. 249 (Jan. 2025) 113500, https://doi.org/10.1016/j.matdes.2024.113500.
[9] G. Xu, V.G. Ataloglou, S.V. Hum, G.V. Eleftheriades, Extreme beam-forming with impedance Metasurfaces featuring embedded sources and Auxiliary Surface wave optimization, IEEE Access 10 (2022) 28670–28684, https://doi.org/10.1109/access.2022.3157291.
[10] V. Joy, Alka Dileep, P. V. Abhilash, R. U. Nair, and H. Singh, "Metasurfaces for Stealth Applications: A Comprehensive Review," Journal of electronic materials, vol. 50, no. 6, pp. 3129–3148, Apr. 2021, doi: Doi:10.1007/s11664-021-08927-3.
[11] A. Sobczyk, A. Karolina Filak-Mędoń, J.S. Kowalczyk, M. Zdrojek, M. Sypek, Ultra-low reflection of sub-THz waves in graphene-based composite with metasurface for stealth technology, Optics Express, Aug. (2024), https://doi.org/10.1364/oe.531259.

[12] S. Zhang, et al., Metasurfaces for biomedical applications: imaging and sensing from a nanophotonics perspective, Nanophotonics 10 (1) (Sep. 2020) 259–293, https://doi.org/10.1515/nanoph-2020-0373.
[13] L. Li, et al., Equivalent circuit models of a bifunctional optical Metasurface for beam splitting and Refractive index sensing, ACS Photonics 10 (8) (Jun. 2023) 2746–2754, https://doi.org/10.1021/acsphotonics.3c00456.
[14] J. Yang, S. Gurung, Subhajit Bej, P. Ni, and Ho Nyung Lee, "Active optical metasurfaces: comprehensive review on physics, mechanisms, and prospective applications," Reports on Progress in Physics, vol. 85, no. 3, pp. 036101–036101, Mar. 2022, doi: Doi:10.1088/1361-6633/ac2aaf.
[15] G. Cai, et al., Compact angle-resolved metasurface spectrometer, Nat. Mater. 23 (1) (Nov. 2023) 71–78, https://doi.org/10.1038/s41563-023-01710-1.
[16] Y. Hu, et al., All-dielectric metasurfaces for polarization manipulation: principles and emerging applications, Nanophotonics 9 (12) (Jun. 2020) 3755–3780, https://doi.org/10.1515/nanoph-2020-0220.
[17] Q. Liu, et al., Incomplete phase Metasurface for wavefront reconstruction, ACS Photonics 10 (8) (Jul. 2023) 2563–2569, https://doi.org/10.1021/acsphotonics.3c00275.
[18] A.C. Tasolamprou, L. Zhang, E.N. Economou, C.M. Soukoulis, T. Koschny, Surface states on photonic crystals as hybrid dielectric Metasurface bound states of the termination layer, ACS Photonics 7 (10) (Sep. 2020) 2842–2849, https://doi.org/10.1021/acsphotonics.0c01083.
[19] W. Lee et al., "Single-layer phase gradient mmWave metasurface for incident angle independent focusing," Scientific Reports, vol. 11, no. 1, Jun. 2021, doi: Doi: 10.1038/s41598-021-92083-5.
[20] M.A. Allodi, P.D. Dahlberg, R.J. Mazuski, H.C. Davis, J.P. Otto, G.S. Engel, Optical resonance imaging: an optical analog to MRI with Subdiffraction-limited capabilities, ACS Photonics 3 (12) (Nov. 2016) 2445–2452, https://doi.org/10.1021/acsphotonics.6b00694.
[21] A. Webb, A. Shchelokova, A.P. Slobozhanyuk, I. Živković, R. Schmidt, Novel materials in magnetic resonance imaging: high permittivity ceramics, metamaterials, metasurfaces and artificial dielectrics, MAGMA 35 (6) (Apr. 2022) 875–894, https://doi.org/10.1007/s10334-022-01007-5.
[22] Z. Hu, Y. Yang, L. Xu, Y. Hao, H. Chen, Binary acoustic metasurfaces for dynamic focusing of transcranial ultrasound, Front. Neurosci. 16 (Sep. 2022), https://doi.org/10.3389/fnins.2022.984953.
[23] J. Lan, Y. Diao, X. Duan, A. Hirata, Planar omnidirectional Wireless power transfer system based on novel Metasurface, IEEE Trans. Electromagn. Compat. 64 (2) (Apr. 2022) 551–558, https://doi.org/10.1109/temc.2021.3123047.
[24] J. Zhao, et al., Wearable optical sensing in the Medical internet of things (MIoT) for pervasive medicine: opportunities and challenges, ACS Photonics 9 (8) (Aug. 2022) 2579–2599, https://doi.org/10.1021/acsphotonics.2c00898.
[25] W. Zhang, et al., Recent Research advances in textile-based flexible power supplies and displays for Smart Wearable applications, ACS Appl. Electron. Mater. (Jul. 2024), https://doi.org/10.1021/acsaelm.4c00606.
[26] N. Ashraf, et al., Intelligent beam steering for Wireless communication using programmable Metasurfaces, IEEE Trans. Intell. Transp. Syst. 24 (5) (May 2023) 4848–4861, https://doi.org/10.1109/tits.2023.3241214.
[27] Y. Zheng et al., "Broadband Achromatic Metalens in the Long-Wave Infrared Regime," vol. 15, no. 2, pp. 1–7, Apr. 2023, doi: Doi:10.1109/jphot.2023.3243409.
[28] Y. Huang et al., "Broadband Achromatic Metalens with Enhanced Field of View for Thermal Image," Journal of Lightwave Technology, pp. 1–7, Jan. 2024, doi: Doi: 10.1109/jlt.2024.3519381.
[29] Y.-X. Xie, G.-B. Wu, W.-Q. Deng, S.-Y. Zhu, C.H. Chan, A 3-D printed ultra-wideband achromatic metalens antenna, IEEE Open Journal of Antennas and Propagation 4 (Jan. 2023) 713–723, https://doi.org/10.1109/ojap.2023.3295834.
[30] J. Chen, H. Chu, Y. Zhang, Y. Lai, M. Chen, D. Fang, Modified luneburg lens for achromatic Subdiffraction focusing and directional emission, IEEE Trans. Antennas Propag. 69 (11) (Jun. 2021) 7930–7934, https://doi.org/10.1109/tap.2021.3083843.
[31] J. Huang, et al., Broadband achromatic metalenses with high focusing efficiency based on inverse design, IEEE Photon. Technol. Lett. 35 (23) (Sep. 2023) 1255–1258, https://doi.org/10.1109/lpt.2023.3314624.
[32] J. Wang, X.-C. Zhao, Y.-N. Jiang, W.-Q. Gu, K.-D. Xu, Optimal design of broadband linear-to-circular polarization conversion metasurface, Mater. Des. 242 (Jun. 2024) 113004, https://doi.org/10.1016/j.matdes.2024.113004.
[33] J. Wang, W.-Q. Gu, X.-C. Zhao, Y.-N. Jiang, K.-D. Xu, Designing broadband cross-polarization conversion metasurfaces using binary particle swarm optimization algorithm, Mater. Des. 247 (Nov. 2024) 113419, https://doi.org/10.1016/j.matdes.2024.113419.
[34] Z. Ding, W. Su, Y. Luo, L. Ye, H. Wu, H. Yao, Machine learning in design of broadband terahertz absorbers based on composite structures, Mater. Des. 233 (Aug. 2023) 112215, https://doi.org/10.1016/j.matdes.2023.112215.
[35] P. Naseri, S.V. Hum, A generative machine Learning-based approach for inverse design of multilayer Metasurfaces, IEEE Trans. Antennas Propag. 69 (9) (2021) 1, https://doi.org/10.1109/TAP.2021.3060142.
[36] H. Wang, Y. Lyu, J. Jiang, H. Zhu, Data-driven inverse design of novel spinodoid bone scaffolds with highly matched mechanical properties in three orthogonal directions, Mater. Des. 251 (Feb. 2025) 113697, https://doi.org/10.1016/j.matdes.2025.113697.
[37] R. Zhu et al., "Phase-to-pattern inverse design paradigm for fast realization of functional metasurfaces via transfer learning," Nature Communications, vol. 12, no. 1, May 2021, doi: Doi:10.1038/s41467-021-23087-y.
[38] C. Jin et al., "Machine learning inverse design of high-strength mid-temperature Ag-based solders," Materials & Design, pp. 113736–113736, Feb. 2025, doi: Doi: 10.1016/j.matdes.2025.113736.
[39] W. Ma, et al., Pushing the limits of functionality-multiplexing capability in Metasurface design based on statistical machine Learning, Adv. Mater. 34 (16) (Mar. 2022) 2110022, https://doi.org/10.1002/adma.202110022.
[40] M. Huang, et al., Machine–learning-enabled metasurface for direction of arrival estimation, Nanophotonics 11 (9) (Jan. 2022) 2001–2010, https://doi.org/10.1515/nanoph-2021-0663.
[41] Z. Wang, et al., Metasurface on integrated photonic platform: from mode converters to machine learning, Nanophotonics 11 (16) (Jul. 2022) 3531–3546, https://doi.org/10.1515/nanoph-2022-0294.
[42] H. Lin, et al., Machine-learning-assisted inverse design of scattering enhanced metasurface, Opt. Express 30 (2) (Jan. 2022) 3076, https://doi.org/10.1364/oe.448051.
[43] W. Zhou, et al., An inverse design paradigm of multi-functional elastic metasurface via data-driven machine learning, Mater. Des. 226 (Jan. 2023) 111560, https://doi.org/10.1016/j.matdes.2022.111560.
[44] "DragonFly IV," Nano Dimension - AME Manufacturing Company. https://www.nano-di.com/dragonfly-iv.
[45] Y. Yang et al., "A Review of Multimaterial Additively Manufactured Electronics and 4-D Printing/Origami Shape-Memory Devices: Design, Fabrication, and Implementation," Proceedings of the IEEE, pp. 1–46, Jan. 2024, doi: Doi:10.1109/jproc.2024.3471849.
[46] J. Zhu, Y. Yang, S. Liao, Q. Xue, Additively Manufactured metal-only waveguide-based millimeter-wave broadband achromatic Reflectarrays, IEEE Trans. Antennas Propag. 71 (7) (May 2023) 6185–6190, https://doi.org/10.1109/tap.2023.3278799.
[47] J. Zhu, et al., Additively Manufactured millimeter-wave dual-band single-Polarization Shared aperture Fresnel zone plate metalens antenna, IEEE Trans. Antennas Propag. 69 (10) (Oct. 2021) 6261–6272, https://doi.org/10.1109/tap.2021.3070224.
[48] J. Zhu, S. Liao, S. Li, Q. Xue, Additively Manufactured metal-only millimeter-wave dual Circularly Polarized Reflectarray antenna with independent control of Polarizations, IEEE Trans. Antennas Propag. 70 (10) (Oct. 2022) 9918–9923, https://doi.org/10.1109/tap.2022.3184474.
[49] M. Pu, et al., Design principles for infrared wide-angle perfect absorber based on plasmonic structure, Opt. Express 19 (18) (Aug. 2011) 17413, https://doi.org/10.1364/oe.19.017413.
[50] Y. Liu, Yu Jian Cheng, Xing Yu Lei, and Peng Fei Kou, "Millimeter-Wave Single-Layer Wideband High-Gain Reflectarray Antenna With Ability of Spatial Dispersion Compensation," IEEE Transactions on Antennas and Propagation, vol. 66, no. 12, pp. 6862–6868, Dec. 2018, doi: Doi:10.1109/tap.2018.2874670.
[51] Y. Zheng, et al., Broadband achromatic metalens in the long-wave Infrared regime, IEEE Photonics J. 15 (2) (Apr. 2023) 1–7, https://doi.org/10.1109/jphot.2023.3243409.
[52] W.T. Chen, A.Y. Zhu, F. Capasso, Flat optics with dispersion-engineered metasurfaces, Nat. Rev. Mater. 5 (8) (Jun. 2020) 604–620, https://doi.org/10.1038/s41578-020-0203-3.
[53] H. Li, Y. Zheng, X. Wu, Q. Cai, 3D model generation and reconstruction using conditional generative Adversarial network, International Journal of Computational Intelligence Systems 12 (2) (2019) 697, https://doi.org/10.2991/ijcis.d.190617.001.
[54] T. Cai et al., "Ultrawideband chromatic aberration-free meta-mirrors," Advanced photonics, vol. 3, no. 01, Dec. 2020, doi: Doi:10.1117/1.ap.3.1.016001.
[55] W. Chen, L. Deng, K.L. Chung, M. Qu, B. Feng, Metasurface-based time-reversal interpolation method for electromagnetic focusing in complex scattering environments, IEEE Trans. Antennas Propag. 72 (7) (Jun. 2024) 5782–5793, https://doi.org/10.1109/tap.2024.3414615.